

Evolution of an initially columnar vortex terminating normal to a no-slip wall

A. Hirsa, J. M. Lopez, S. Kim

Abstract The early evolution of an initially columnar vortex normal to a solid wall was examined. The vortex was generated by a pair of flaps in a water tank. Detrimental effects from the wall during the vortex generation were avoided by producing the vortex normal to a free surface and subsequently bringing a horizontal plate into contact with the surface. Digital particle image velocimetry (DPIV) measurements of the velocity and vorticity, together with laser induced fluorescence (LIF) visualizations, in a meridional plane revealed a toroidal structure with the appearance of an axisymmetric vortex breakdown bubble. Agreement was found between the measurements and numerical simulations of the axisymmetric Navier–Stokes equations. The results show that the flow in the effusive corner region is dominated by a Bödewadt-type spatially oscillatory boundary layer within the core region and a potential-like vortex boundary layer at large radii. The toroidal structure results from the interaction between these two boundary layers, leading to the roll up of a dominant shear layer within the Bödewadt structure, and does not develop from the columnar vortex itself.

1

Introduction

The interaction of a vortex with a rigid wall is of interest for its prevalence in many practical situations, such as vortex chambers, and in geophysical flows, such as tornado/ground interactions. Vortex/endwall flows are also of fundamental interest and the subject has a long history of theoretical and experimental investigation which is ongoing. The first study to examine the production of secondary flow induced by the interaction of a vortex with a rigid boundary was that of Taylor (1950). Taylor's theoretical study only applied to the boundary layer formed away from the core, as have most other such studies, e.g., see Burggraf et al. (1971) and Belcher et al. (1972). These have relied on boundary layer approximations to the governing equations, and the question largely remains as to how the flow evolves in the effusive corner region, where the boundary layer flow is turned into the axial direction. For a recent review of rotating flows with axis normal to a no-slip wall, see Lugt (1996).

The nature of the flow in the effusive corner is far more complicated than that in just a single boundary layer, or a vortex core. This is a region where the usual boundary layer approximation is not valid as the interaction involves two boundary layer type flows that are perpendicular to each other so gradients in one direction do not dominate those in the other. For the vortex, the flow in a small region near the axis is dominated by viscous forces. This is the region where the vortex flow is regularized, and is in this sense a boundary layer type flow. The secondary flow induced by the bending of the vortex lines into a thin region near the wall results in an endwall boundary layer. This secondary boundary layer flow has a strong inward radial mass flux, and the nature of the interactions of the endwall boundary layer with the vortex subcore requires a treatment where the viscous forces are included.

There are fundamental questions that remain unanswered about the interaction of a vortex terminating at a solid wall, as the temporal evolution of the corner flow is not well understood. Maxworthy (1972) has pointed out that there seems to be no way to study this region other than through computations of the nonlinear governing equations. Maxworthy (1973) presents a schematic model of the interactions in the effusive corner region, but concludes that the interactions in this region are probably more complicated than suggested by the model, and that detailed measurements are needed to unravel the delicate balance of forces. In Maxworthy's (1972) experiments, as

Received: 16 September 1998/Accepted: 13 October 1999

A. Hirsa, S. Kim¹
Department of Mechanical Engineering
Aeronautical Engineering and Mechanics
Rensselaer Polytechnic Institute
Troy, NY 12180-3590, USA

J. M. Lopez
Department of Mathematics
Arizona State University
Tempe, AZ 85287-1804, USA

¹ Present address:
Hyundai Engineering and Construction Co., Ltd., Seoul, S. Korea

Correspondence to: A. Hirsa (hirsaa@rpi.edu)

We would like to thank Mr. J.M. Mortzheim for assisting with some of the DPIV analysis. This work was partially supported by the Office of Naval Research through Grant No. N000149410062, monitored by Dr. E.P. Rood, and Grant No. N000149611063, monitored by Drs. F.L. Herr and D.B. Trizna, and by NSF Grant Nos. DMS-9512483 and DMS-9706951.

well as more recent ones (e.g., Phillips 1985), a toroidal recirculation region is observed in the neighborhood of the effusive corner that has visual characteristics in common with the vortex breakdown of columnar vortices. Based on these observations, it has been suggested that vortex breakdown plays a role in the balance of forces in the effusive corner region. However, it is not clear whether the toroidal structure results directly from the disruption of the columnar vortex.

To permit direct measurements, a new flow apparatus has been utilized to generate an initially columnar vortex, with vortex lines terminating normal to the endwall, to study the temporal evolution in the effusive corner region. The problem of the no-slip boundary continuously affecting the vortex during its generation process has been circumvented by generating the vortex normal to a free surface, i.e. an air/water interface (see Hirska et al. 1995). Once the columnar vortex has been generated, the no-slip boundary condition is imposed essentially instantaneously and the evolution of the vortex/endwall interaction is then studied. A schematic of the columnar vortex generator is presented in Fig. 1. Previous experimental studies of the corner region (e.g., Maxworthy 1972; Phillips 1985) were concerned with situations where the circulation of the outer flow and an equilibrium boundary layer flow were maintained. Here, we are concerned with the evolution of vortex lines and the secondary flow that results solely from the interaction of the vortex with the wall. Other investigations (e.g., Turner

1966; Ward 1972; Church et al. 1979; Snow 1982; Howells and Smith 1983; Wilson and Rotunno 1986; Howells et al. 1988; Fiedler 1994) have been of systems where there already existed considerable meridional flow before the vortex was generated and the interaction in the effusive corner region was investigated. The nature of the extraneous meridional flows are expected to alter the interaction.

Although the flow in the effusive corner achieved in most laboratory experiments appears to be three dimensional, we expect that the evolution of the corner flow involves only a strictly axisymmetric process. This hypothesis is tested via numerical experiments where the unsteady axisymmetric Navier–Stokes equations are solved using a robust and well-tested numerical code to determine whether it captures the essence of the interactions and evolution as measured in the experiments.

2

Experimental apparatus and techniques

The experiments were conducted using a columnar vortex generator, schematically shown in Fig. 1. The vortex generator consisted of a pair of vertically-oriented stainless steel flaps in a 25 cm diameter Plexiglas water tank. The tank was filled with distilled water at 24 °C (kinematic viscosity $\nu = 9.1 \times 10^{-3} \text{ cm}^2/\text{s}$) which was passed through a short wavelength (187 nm) ultraviolet filter (Ideal Horizons, model SR1). The cylindrical tank was placed inside a larger square-shaped water tank in order to eliminate the optical distortion caused by viewing through the curved wall. Each flap (4.4 cm wide, 25.4 cm high, and 0.2 cm thick) extended from the bottom of the tank to 0.2 cm above the free surface. The center of rotation of each flap was 4.5 cm from the centerline (z -axis). The flaps were initially 3° ahead of a radially opposing position, and were co-rotated a total of 66° , thus forming the sides of a rectangle, $8 \times 4.4 \text{ cm}$, with the vortex in its center, as illustrated in Fig. 1a. The flap rotation was achieved by a stepper motor (Superior Electric, model M063-LE06) through a set of pulleys and a timing belt. The stepper motor was controlled by a programmable micro-indexer/driver (Superior Electric, model 6180-EPI-125) and a personal computer. The rotation of the flaps consisted of a relatively large constant acceleration, followed by a deceleration profile which simulated the vortex sheet distribution behind an elliptically loaded wing (Locke et al. 1993). The resulting vortex sheet shed from each flap rolled up smoothly into a single columnar vortex at the center of the tank.

In order to eliminate the strong upward axial motion induced at the bottom of the vortex by the tank floor, a thin rotor with a diameter of 2.4 cm and rotation rate of 4.1 rad/s was utilized. The rotor diameter and speed were experimentally optimized so that disturbances from the bottom did not reach the mid-depth for at least 30 s after the generation of the vortex. A flexible wiper attached to the bottom of each flap maintained contact with the tank floor as the flaps traveled past the rotor, further reducing secondary flows at the bottom of the vortex.

Near the completion of the flap rotation process, a rigid no-slip boundary condition was imposed at the top

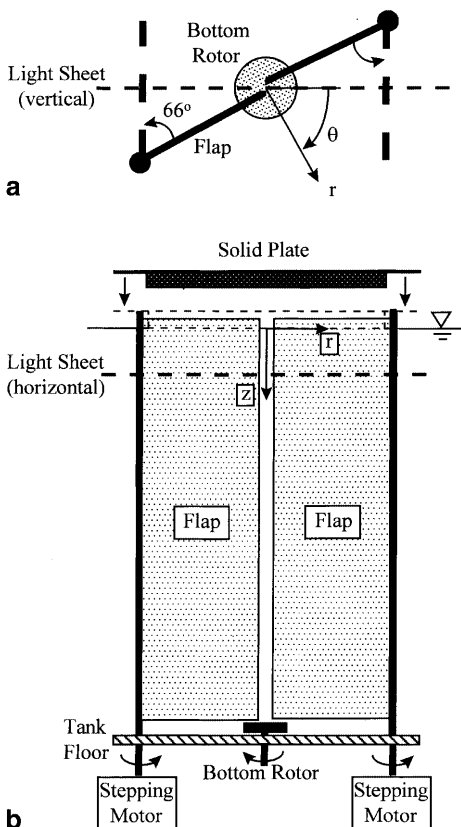


Fig. 1a, b. Schematic of the experimental apparatus; a top view, b front view

of the vortex, as illustrated in Fig. 1b. A 7×5 cm Plexiglas plate, which was partially supported by the flaps, dropped down 0.2 cm onto the free surface after the flaps had rotated 62° . Prior to each experiment, the plate was coated with a thin film of water, thereby upon falling on the free surface complete wetting would occur without the trapping of any air bubbles. Additionally, prior to each experiment the free surface was cleaned using surface suction. The absence of surface active contaminants on the air/water interface ensured columnar vortex behavior before the imposition of the no-slip condition (Hirsa et al. 1995).

The interaction of the columnar vortex with the solid wall was examined through flow visualization and measurements of the velocity field. Flow visualization was achieved by the planar laser-induced fluorescence (LIF) technique, as described earlier (Hirsa et al. 1995). The velocity field was measured using digital particle image velocimetry (DPIV, see Willert and Gharib 1991). The present technique has been described in detail elsewhere (Logory et al. 1997; Hirsa et al. 1997) and only a brief description of the present system configuration is given here. The illumination for DPIV was provided by an Nd:YAG laser (Continuum, model NY-6030) operating at 30 Hz. The images were obtained with a CCD camera (Texas Instruments, model MC1131P, along with a 58 mm $f/1.4$ Nikkor lens), and digitized by a frame grabber (Epix, model 12-16 Meg) and a personal computer. A method of spatial resolution enhancement (Logory et al. 1996) was utilized with sampling window sizes of 64×64 , 32×32 , and 16×16 pixels. The analysis was performed with overlapping of zero and 50% of the sampling windows for horizontal and vertical planes, respectively, but in either case, approximately 10^3 independent velocity vectors are obtained in each measurement. Polycrystalline particles (Optimage, s.g. 0.98–1.02) with a volume-average diameter of $30 \mu\text{m}$ at 1.5×10^3 particles/ml were utilized in the experiments. The uncertainties in the present DPIV measurements were estimated to be $\pm 2\%$ and $\pm 4\%$ (of maximum value) for velocity and vorticity, respectively. Further details of the experimental apparatus and procedures are given in Kim (1996).

3

Laboratory measurements

Measurements were made initially of the vortex terminating at a (clean) free surface, i.e. without the imposition of the solid wall, in order to quantify the underlying flow field and establish that the vortex is columnar and without meridional flow. Figure 2 presents measurements in a cross-sectional plane ($r-\theta$ also $x-y$) at a dimensional depth of $\tilde{z} = 5$ cm. Note, all variables denoted with a tilde ($\tilde{\cdot}$) are dimensional. These measurements were taken at the dimensional time $\tilde{t} = 5$ s, where $\tilde{t} = 0$ is defined as the time when the flaps stop rotating. Figure 2a shows visualization of the flow obtained through LIF using a horizontally-oriented laser sheet. The dye streak pattern shows that the vortex sheet shed from each flap smoothly roll up and amalgamate into a single vortex which appears to be stable. The flaps are located on the left and right sides of the field of view, at $\tilde{x} = \pm 4$ cm. The elliptic appearance of the vortex is due in part to the lack of azimuthal symmetry which is present from the start of the vortex sheet roll up process, consisting of an inviscid effect caused by the straightening of streamlines near the flaps as well as a viscous effect due to the no-slip condition on the flaps. The dye visible on the left and on the right edge of the image is associated with the boundary layer that is induced on the flaps by the vortex flow at the center. The bright spot at approximately the 11 o'clock position is due to light scattered from excess dye deposited off-axis and at a depth greater than 5 cm.

Measurements of the velocity and the associated axial vorticity for the same time and location are presented in Fig. 2b and c, respectively. It should be noted that the LIF image shown in Fig. 2a was taken from above the free surface looking downward, whereas the images for the DPIV measurements, e.g. Fig. 2b, were taken looking up through the bottom of the water tank, in order to eliminate any distortion caused by free surface deformations. Thus, the vortex has the opposite sense of rotation in Fig. 2a as compared to Fig. 2b and c. The velocity measurements show that the streamlines are straightened in the vicinity of the flaps. The Reynolds number based on the vortex core radius, r_c , and the azimuthal velocity at the core

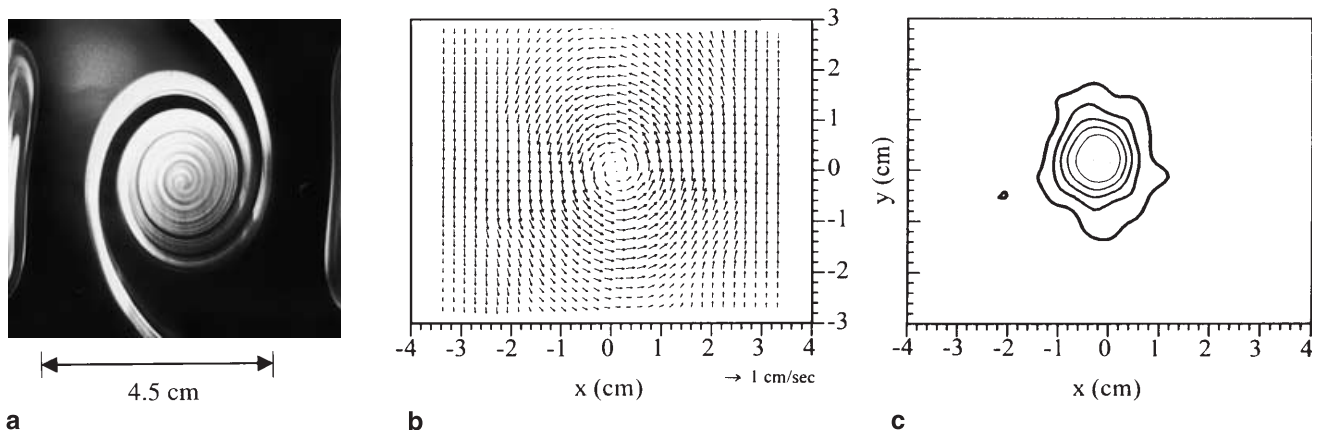


Fig. 2a–c. Measurements in the cross-sectional plane in the absence of the solid wall, at a depth of 5 cm and time of 5 s; a LIF photograph, and DPIV measurements of b the horizontal

velocity and c the corresponding axial vorticity. The vorticity contour levels start at 1 s^{-1} (thickest line) and are in increments of 1 s^{-1} , and the maximum vorticity is 6.38 s^{-1}

radius, V_c , and kinematic viscosity, ν , ranges from $Re = r_c V_c / \nu = 125$ in the direction normal to the flaps, to 100 in the direction parallel to the flaps, with an overall average of about 112.

The nondimensionalized azimuthal velocity profile in the y -direction (i.e. parallel to the flaps) is shown in Fig. 3a and the profile in the x -direction (normal to the flaps) is shown in Fig. 3b. Each plot shows the instantaneous velocity profiles for two depths, $\tilde{z} = 2$ and 5 cm, at $\tilde{t} = 5$ s. The data for each depth was obtained from separate realizations of the flow. Since the core radius and velocity have numerical values very close to unity (in the cgs system), the nondimensionalized depths shown in Fig. 3 are $z = 2$ and 5 and the time is $t = 5$. The radial profile of the tangential velocity can be described by a general form:

$$v(r) = Br^{-n}(1 - \exp(-Ar^{1+n})) , \quad (1)$$

where $B = (1 - \exp(-A))^{-1}$ and n depends on the azimuthal angle (relative to the flaps). The profile (1) is normalized by choosing A so that $v(1) = 1$ and $v'(1) = 0$. The $n = 1$ case corresponds to the classic Oseen vortex; it has been studied by Burgers (1948) and Rott (1958). The

data shows that in the direction parallel to the flaps (Fig. 3a) the velocity decreases rapidly outside of the core and a value of $n = 1.3$ provides the best fit to the vortex described by (1). Figure 3b shows that the velocity decrease outside of the core in the direction normal to the flaps is comparatively slow, with a corresponding $n = 0.4$. The primary flow ($\Gamma = rv$) is qualitatively different for values of n either side of $n = 1$. At early times and for $n = 1$, $\Gamma \rightarrow \text{constant}$ for $r > r_c$, so that the primary flow (outside of boundary layers) becomes irrotational asymptotically fast. For $n < 1$, the axial vorticity $1/r \partial \Gamma / \partial r > 0$ for all r , so that as n decreases from 1, there is more rotational flow at large radii. For $n > 1$, on the other hand, there is a radius greater than r_c at which the axial vorticity changes sign. Note that the azimuthal velocity v does not reverse direction, only the radial gradient of $\Gamma = rv$ changes sign. So the vortex structure for n either side of 1 is fundamentally different from $t = 0$ onwards. For $n = 1$, all the vortex lines are essentially contained within a radius, which is approximately equal to r_c at very early times, and are directed in the positive axial direction; the flow outside this radius is asymptotically irrotational. For $n < 1$, there is no radius beyond which the flow is irrotational and all the vortex lines are directed in the positive axial direction for all r . With $n > 1$, there is a radius whose value is an increasing function of time, below which the vortex lines are directed in the positive axial direction and above which the vortex lines are directed in the negative axial direction. These differences in the form of the primary flow have direct consequences on the eventual structure of the secondary flow following the interaction with the no-slip wall.

Both plots in Fig. 3 also show that when the top no-slip boundary is not imposed, there is good agreement between the velocity measurements at the two depths. The columnar nature of the vortex is also evident in the LIF images taken in the meridional plane, shown in Fig. 4. Figure 4 confirms that the upper half of the vortex generated by the flaps remains columnar at least until $t = 20$.

The effect of the no-slip wall is presented in the following figures. Figure 5 shows the velocity and the corresponding axial vorticity in a cross-sectional (horizontal) plane at depth $z = 1$ and various times. At $t = 0$ (Fig. 5a, b) the flaps stop and the measurements show that at this depth and time the rigid wall, which was imposed less than 3 time units earlier, has little influence. The flow field appears to be similar to that of the columnar vortex terminating at a free surface (Fig. 2). Figure 5c, d shows that at $t = 10$ the magnitude of the (horizontal) velocity near the center is rapidly decreasing with time and by $t = 20$, Fig. 5e, f shows a large region at the center of the core where the horizontal velocity is almost zero. Figure 5 also shows that the axial vorticity significantly decreases with time at this depth, and by $t = 20$ the peak axial vorticity appears in a nearly ring-shaped region. The axial vorticity at the center is significantly smaller than either the maximum axial vorticity for this case or the axial vorticity at the center of the core for the case without the wall at the same instant and depth.

Figure 6 presents DPIV measurements at $z = 2$, i.e. twice the depth of the previous figure. At this depth, the

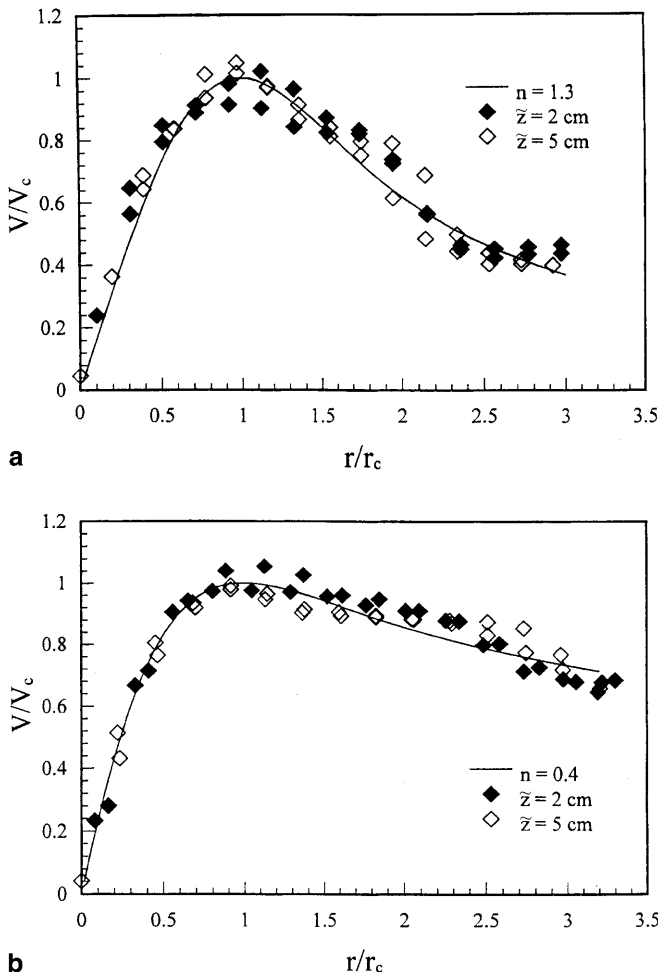


Fig. 3a, b. Radial profiles of the tangential velocity in the absence of the solid wall, and normalized with the core velocity (V_c) and the core radius (r_c); a along the y -axis (i.e. $\theta = 90^\circ$ and 270°) b along the x -axis (i.e. $\theta = 0^\circ$ and 180°)

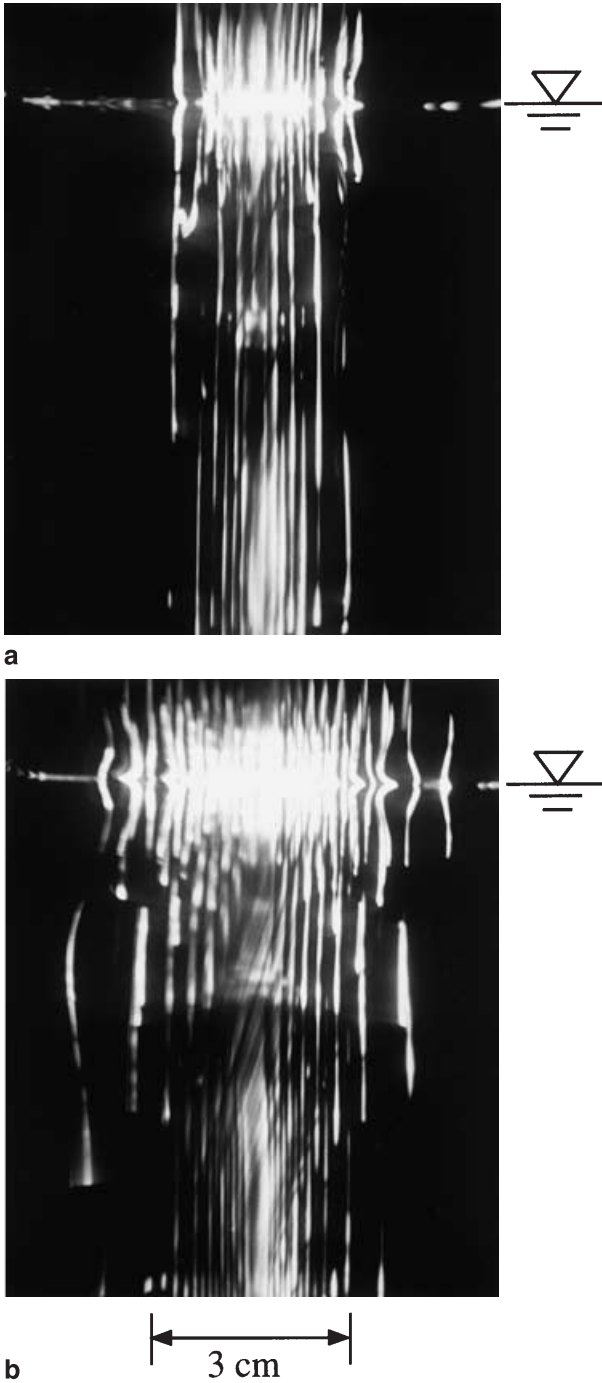


Fig. 4a, b. LIF photographs in a meridional plane in the absence of the solid wall; a $\tilde{t} = 0$ s, b $\tilde{t} = 20$ s. Note the mirror image visible at the top of each photograph is due to total internal reflection from the free surface

effect of the wall is much less significant than at $z = 1$. Figure 6a, b shows the vortex at $t = 0$; the maximum axial vorticity is similar to the case without the wall. The diminishing influence of the endwall with increasing depth is evident in Fig. 6c, d which shows the vortex at $t = 10$. The maximum axial vorticity remains close to the no-wall case, and is significantly greater than at depth $z = 1$. Similarly, at $t = 20$ (Fig. 6e, f) the maximum axial vorticity remains much larger than at $z = 1$, and unlike at the shallower

depth, the maximum occurs at the center. The presence of a small amount of wobble (less than 2 degrees) is evident in the measurements presented in Figs. 5 and 6, i.e. although the vortex is essentially columnar, it is not perfectly cylindrical and its axis is not perfectly aligned with the co-ordinate axis. This means that the axis of the vortex can be slightly tilted at a small angle relative to the meridional plane on which the DPIV measurements are taken, so that the axial component of vorticity times the sine of this angle makes a small (<3.5%) contribution to the azimuthal component, presented below (and in the same way, we miss a small part of the azimuthal component due to the misalignment).

The structure of the flow in the effusive corner is best viewed in the meridional plane. A sequence of DPIV measurements made in a vertical plane are presented in Fig. 7. The sequence of LIF images included in Fig. 7 are from a separate realization of the flow. A strong radial flow directed towards the center is evident near the wall. In the vicinity of the vortex core, the flow turns downwards away from the wall. The boundary layer azimuthal vorticity is too thin to be seen clearly (i.e. resolved) at $t = 5$, shown in Fig. 7c. A second layer of azimuthal vorticity, of opposite sign to that associated with the region closest to the wall, is caused by the bending of the vortex lines as they approach the no-slip wall, and result in the formation of a toroidal region of azimuthal vorticity. It should be noted that the sign of the azimuthal vorticity for the left side of the flow has been switched in the plots of Fig. 7(c, f, i, l) for aesthetic reasons. A third layer of azimuthal vorticity with alternating sign is visible as early as $t = 5$. The azimuthal vorticity layer nearest the wall begins to be resolved by $t = 10$, as shown in Fig. 7f. The primary toroidal structure retains its form and position, but grows larger with time (at least for $t \leq 20$). Also, the third layer of azimuthal vorticity is larger and stronger than at $t = 5$. The meridional velocity vector plot, Fig. 7e, shows that by this time a nearly stagnant region forms at the center at depth $z \approx 1$ (the same time and depth that the horizontal velocity vanished, see Fig. 5). The flow above and below this zone is directed away from the surface. The extent of the stagnation zone grows, and by $t = 15$ covers a region between $1 < z < 2$. At the final time, $t = 20$, the layered structure of the vorticity is evident in Fig. 7l, as is the quasi-steady nature of the primary toroidal structure. When comparing the LIF images with the DPIV measurements, we must keep in mind that the flow is evolving in time and so the appearance of the dye-lines need not resemble the instantaneous streamlines or vortex lines (Hama 1962).

4 Numerical simulations

Computations of the unsteady axisymmetric Navier-Stokes equations were performed to determine the extent to which the experimental results can be described by axisymmetric processes. Where the two agree, we can use the complimentary information derived from each to further elucidate the physics of the process. Also, measurements of the complete flowfield are not practical, and the dynamic range of the measurement technique limits

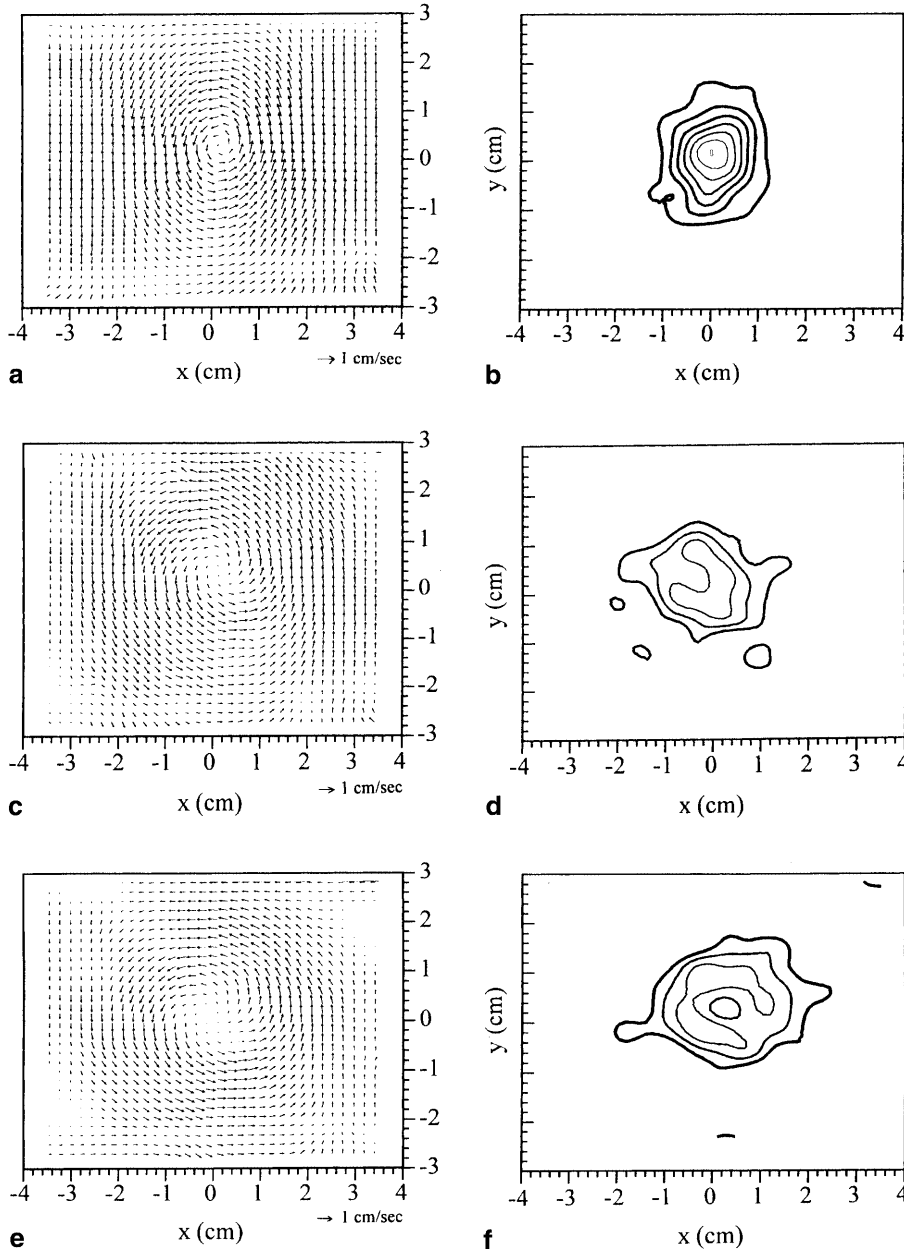


Fig. 5a-f. DPIV measurements of **a** the horizontal velocity and **b** the corresponding axial vorticity, in a cross-sectional plane 1 cm away from the imposed solid wall; **a, b** $\tilde{t} = 0$ s, **c, d** $\tilde{t} = 10$ s, **e, f** $\tilde{t} = 20$ s. The vorticity contour levels start at 1 s^{-1} (thickest line), and are in increments of 1 s^{-1} , and the maximum values of vorticity are: **b** 8.48 s^{-1} , **d** 4.13 s^{-1} , **f** 3.68 s^{-1}

the resolution of the data, so it is very useful to obtain the details of the flow from the computations, particularly near the wall. The numerical code used in this study has been employed in other applications with vortex/endwall interactions (e.g., Lopez 1996; Lopez and Weidman 1996; Lopez and Shen 1998) and only a brief description is presented here.

It is convenient to write the Navier–Stokes equations using a cylindrical polar coordinate system (r, θ, z) . For axisymmetric flow, there exists a Stokes streamfunction ψ and the velocity vector in cylindrical polars is

$$(u, v, w) = \left(-\frac{1}{r} \frac{\partial \psi}{\partial z}, \frac{\Gamma}{r}, \frac{1}{r} \frac{\partial \psi}{\partial r} \right),$$

where the angular momentum Γ has been introduced (Γ is proportional to the circulation). This form of the velocity automatically satisfies the continuity equation. The corresponding vorticity field is

$$(\xi, \eta, \zeta) = \left(-\frac{1}{r} \frac{\partial \Gamma}{\partial z}, -\frac{1}{r} \nabla_*^2 \psi, \frac{1}{r} \frac{\partial \Gamma}{\partial r} \right),$$

where

$$\nabla_*^2 = \frac{\partial^2}{\partial z^2} + \frac{\partial^2}{\partial r^2} - \frac{1}{r} \frac{\partial}{\partial r}.$$

Note that Γ plays the role of a streamfunction for the meridional vorticity field. In other words, contours of Γ in a meridional plane are cross-sections of vortex surfaces (vortex lines), just as contours of ψ are cross-sections of streamsurfaces (streamlines). These give the local direction of the vorticity and velocity vectors in the plane, respectively, and the azimuthal components of the vectors give the degree to which the vectors are directed out of the plane.

The axisymmetric Navier–Stokes equations, in terms of ψ , Γ and η , are:

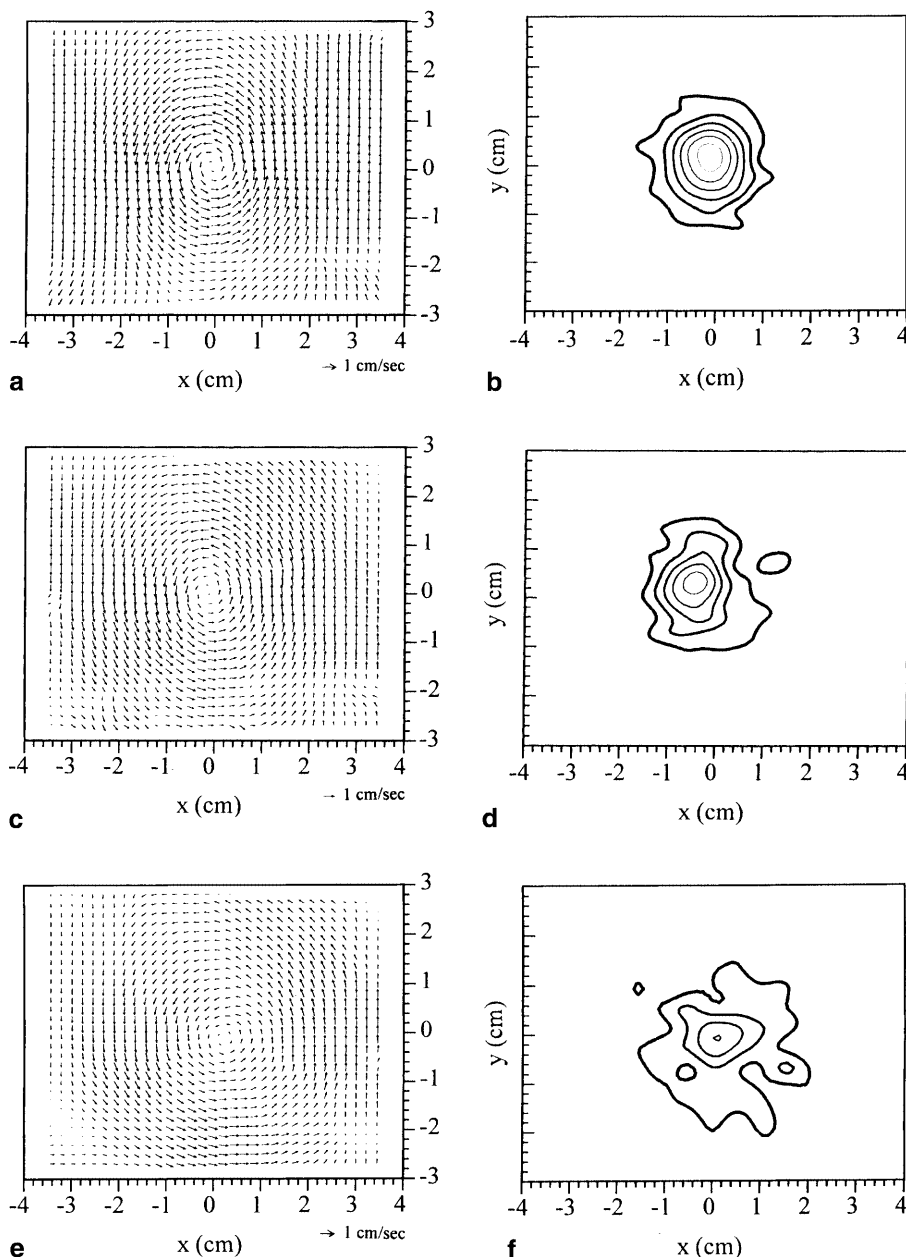


Fig. 6a-f. Same as Fig. 5, except at depth of 2 cm from the wall; the maximum value of vorticity are: **b** 7.48 s^{-1} , **d** 6.11 s^{-1} , **f** 4.87 s^{-1}

$$\frac{D\Gamma}{Dt} = \frac{1}{\text{Re}} \nabla_*^2 \Gamma, \quad (2)$$

$$\frac{D\eta}{Dt} + \frac{1}{r^2} \frac{\partial \psi}{\partial z} \eta - \frac{1}{r^3} \frac{\partial \Gamma^2}{\partial z} = \frac{1}{\text{Re}} \left(\nabla_*^2 \eta - \frac{1}{r^2} \frac{\partial \eta}{\partial r} \right), \quad (3)$$

where

$$\nabla_*^2 \psi = -r\eta, \quad (4)$$

$$\frac{D}{Dt} = \frac{\partial}{\partial t} - \frac{1}{r} \frac{\partial \psi}{\partial z} \frac{\partial}{\partial r} + \frac{1}{r} \frac{\partial \psi}{\partial r} \frac{\partial}{\partial z},$$

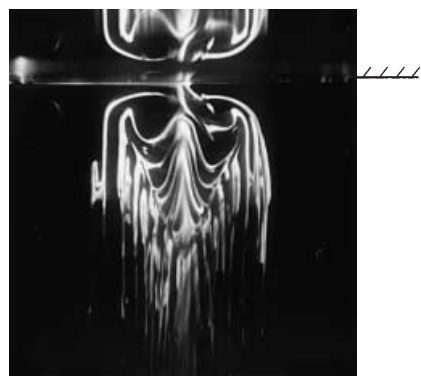
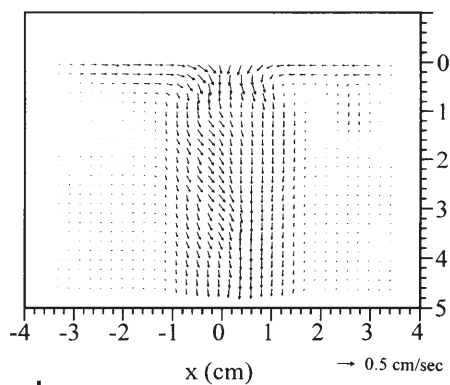
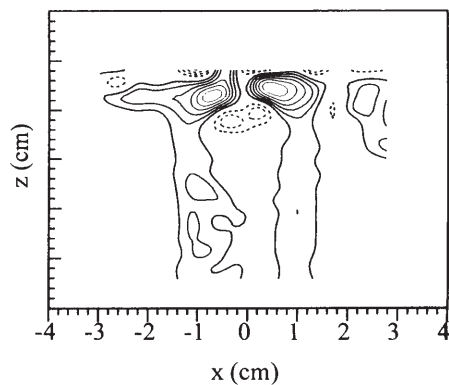
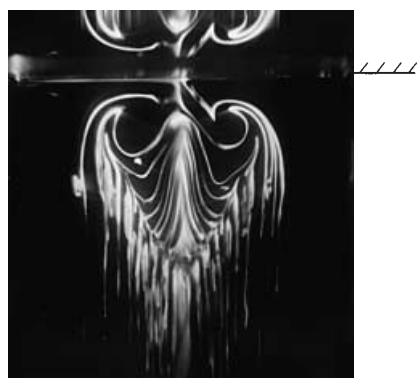
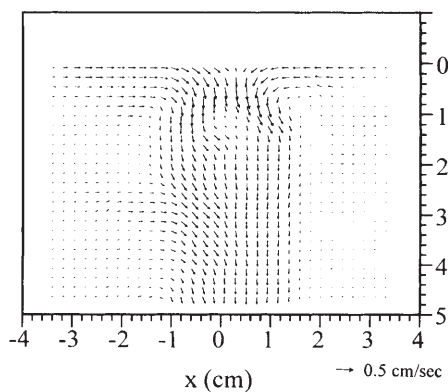
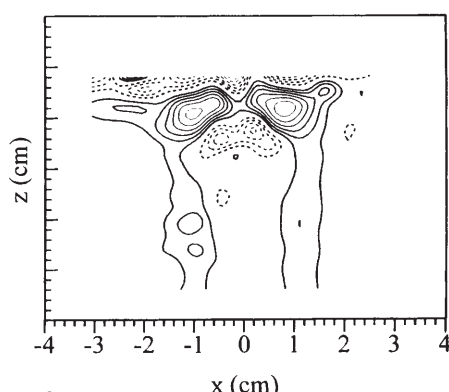
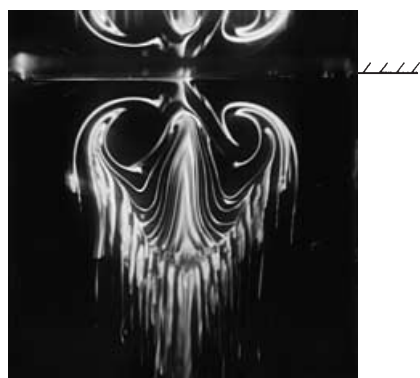
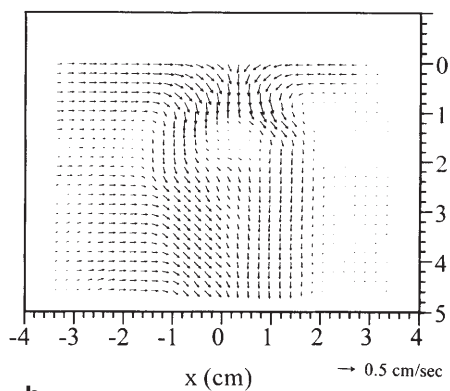
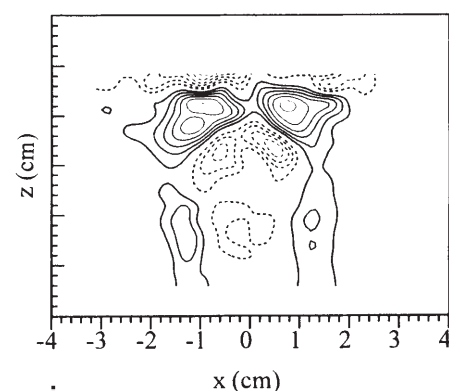
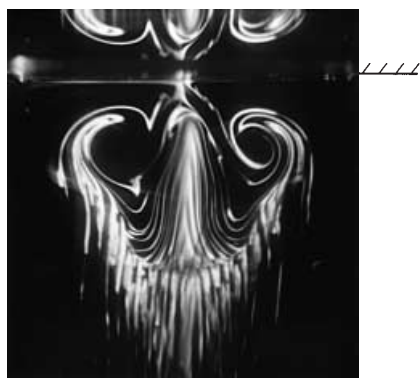
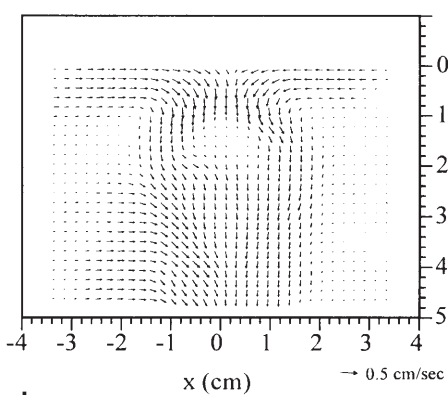
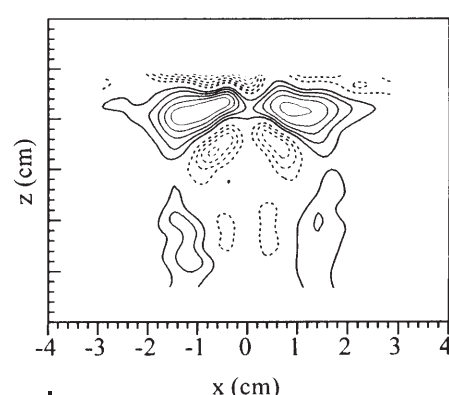
$$\nabla^2 = \frac{\partial^2}{\partial z^2} + \frac{\partial^2}{\partial r^2} + \frac{1}{r} \frac{\partial}{\partial r}.$$

The core radius r_c and the azimuthal velocity at $r = r_c$, V_c , of the initial columnar vortex are used to define the Reynolds number

$$\text{Re} = \frac{r_c V_c}{\nu},$$

where ν is the kinematic viscosity. Equations (2)–(4) are solved using a second-order accurate in both time and space finite-difference scheme, as detailed in Lopez and Weidman (1996) and Lopez and Shen (1998).

The boundary conditions correspond to an enclosed circular cylinder. The radius and height of the cylinder influence the radial velocity in the endwall boundary layers. In the experiment, the presence of the flaps effectively reduces the cylinder radius, but not uniformly in the azimuth and we have no direct way to determine their effect. Computations with a variety of cylinder diameters and heights are presented. A bottom rotor of the same size and speed (non-dimensionalized) as that corresponding to the experiment is incorporated. The presence of the rotating disk provides stretching of the vortex lines and was used in

**a****b****c****d****e****f****g****h****i****j****k****l**

◀ Fig. 7a–l Measurements in the meridional plane of the vortex interacting with the solid wall; a LIF photograph, and DPIV measurements of b velocity and c the corresponding azimuthal vorticity; a–c $t = 5$ s, d–f $t = 10$ s, g–i $t = 15$ s, j–l $t = 20$ s. The vorticity contour levels start at $\pm 0.5 \text{ s}^{-1}$ (thickest lines), and are in increments of 0.5 s^{-1} , and the minimum and maximum values of vorticity are, respectively: c -1.94 and 3.47 s^{-1} , f -3.42 and 3.33 s^{-1} , i -3.32 and 3.21 s^{-1} , l -3.55 and 3.07 s^{-1} (solid lines are positive and broken lines are negative contours)

the experiments to help stabilize the flow. The initial conditions at $t = 0$ correspond to a columnar vortex with zero meridional flow, i.e. $(0, v, 0)$ with v given by Eq. (1) and parameters corresponding to those in the experiment. At that instant, the vortex becomes aware of the presence of solid, stationary endwalls and sidewall, and the bottom rotor. The corresponding boundary conditions are:

- (i) at the stationary, rigid sidewall ($r = R$): $\psi = 0$, $\Gamma = 0$, and $\eta = -1/R\partial^2\psi/\partial r^2$,
- (ii) at the axis ($r = 0$): $\psi = 0$, $\Gamma = 0$, and $\eta = 0$,
- (iii) at the stationary, rigid top endwall ($z = 0$): $\psi = 0$, $\Gamma = 0$, and $\eta = -1/r\partial^2\psi/\partial z^2$, and
- (iv) at the stationary, rigid bottom endwall ($z = Z$): $\psi = 0$, $\Gamma = 0$, and $\eta = -1/r\partial^2\psi/\partial z^2$, except over $0 \leq r \leq 1.25$ (the bottom rotor) where $\Gamma = 4r^2$.

The evolution of the flow depends on both the dynamic governing parameters (the Reynolds number Re and structure of the initial columnar vortex n) and the geometric parameters (the cylinder radius R and height Z). The enclosed geometry and the presence of the rotating disk on the bottom endwall influence the long-time behavior of the flow; however, in this study we are primarily concerned with the early-time evolution of the flow in the effusive corner region following the initial interaction of the columnar vortex with a no-slip wall normal to its axis. For short times, this evolution depends on the local structure of the vortex flow, and the length of time over which this evolution is essentially independent of the confining geometry depends on the dimensions of the cylinder relative to the vortex core radius. We shall illustrate this for a vortex flow of $Re = 125$ with $n = 0.4$, considering cylinders of various radii R and heights Z , and compare the flows in the effusive corner regions at time $t = 20$. The results are qualitatively similar for flows with different Re and n . These results are summarized in Fig. 8, where contours of the azimuthal vorticity η (the induced secondary flow) in the effusive corner region ($r < 4$ and $z < 3$) are plotted. The contour levels are linearly spaced with $\delta\eta = 0.5$, the solid contours are positive (negative) and the broken contours are negative (positive) on the right (left) half of the plots. Computations were performed only in the meridional plane $r \in [0, R]$, $z \in [0, Z]$, but the plots also show a reflection about $r = 0$ for clarity.

Figure 8a, b, and c all have $Z = 25.5$ with R doubling from 4.25 to 8.5 to 17. It is clear that for a vortex with $Re = 125$ and $n = 0.4$, by time $t = 20$ the proximity of the cylinder sidewall at $R = 4.25$ has a substantial effect on the secondary flow, whereas comparing the flows in the cylinders with $R = 8.5$ and 17, the effects have not manifested

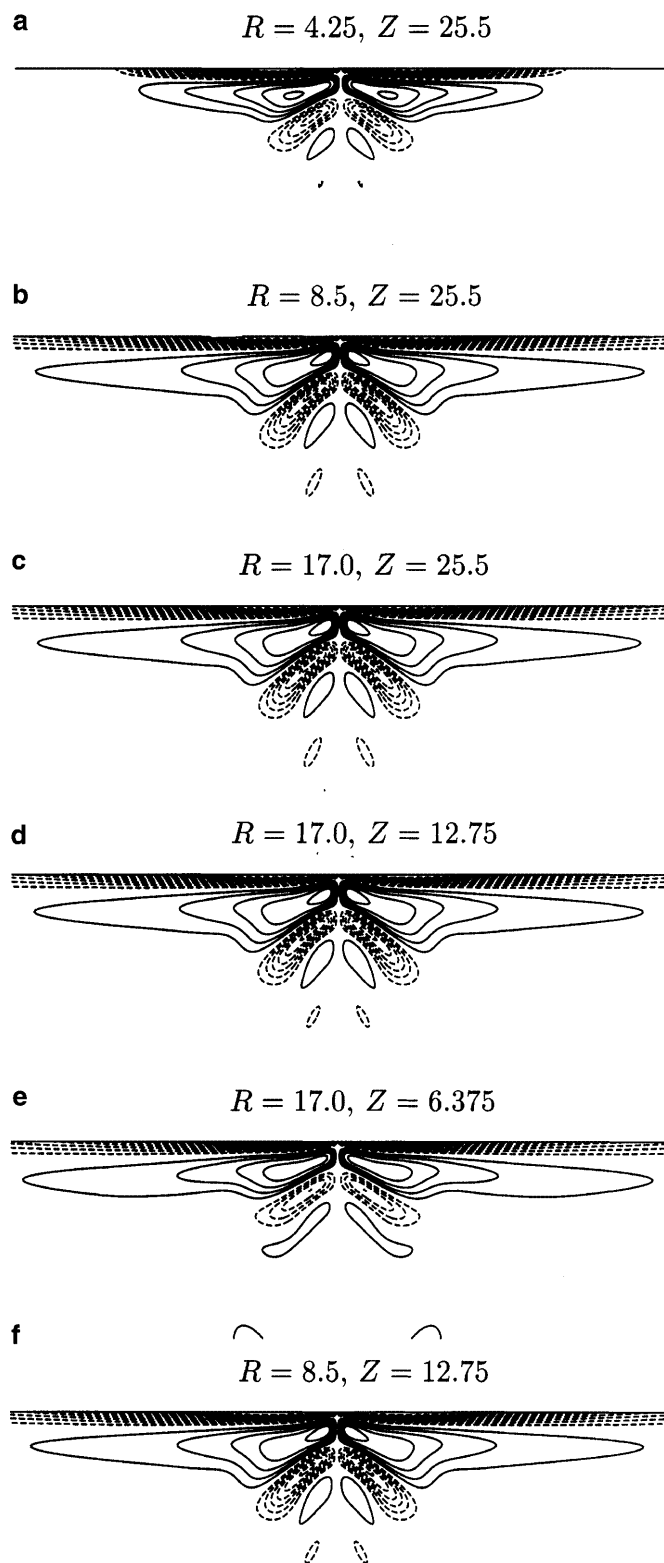


Fig. 8a–f. Contours of η for $Re = 125$, $n = 0.4$ at $t = 20$ in the effusive corner region for calculations with cylinder radius R and height Z as indicated. Solid lines are positive and broken lines are negative contours, and the contour increments are in uniform steps of 0.5

themselves by this time; the evolution of the secondary flow up to this time is independent of the cylinder radius, for $R \geq 8.5$. In Fig. 8c, d, and e, we see that with fixed

$R = 17$ and the height halved from 25.5 to 12.75 to 6.375, that $Z = 6.375$ has an influence on the evolution by $t = 20$, but that the $Z = 12.75$ and 25.5 evolutions of η are essentially the same. Figure 8f shows the case for $R = 8.5$ and $Z = 12.75$; comparing this with Fig. 8c for the case $R = 17$ and $Z = 25.5$, we see that up to $t = 20$, the evolution of the secondary flow is not affected by the dimensions of the cylinder so long as the cylinder radius is greater than about 8.5 and its height greater than about 12.75. The computations of the evolution of the flow in the effusive corner region presented in the sequel are for a cylinder with $R = 17$ and $Z = 25.5$.

Figure 9 shows the vortex lines (contours of Γ) in the effusive corner region for $Re = 125$ at time $t = 20$ for (a) $n = 0.4$, (b) $n = 1.0$, and (c) $n = 1.3$. With the no-slip wall at $z = 0$, the vortex lines cannot be directed in the axial direction in the vicinity of the wall; they are directed asymptotically parallel to the wall as $z \rightarrow 0$, thus producing the vortex endwall boundary layer. The local curvature of the vortex lines (Γ) to a large extent determines the induced secondary flow in the endwall boundary layer and the effusive corner region. Figures 10, 11, and 12 present contours of η in this region at various times for $n = 0.4$, 1.0, and 1.3 respectively. From Fig. 9a, we see that in the endwall boundary layer, the axial gradients in Γ are largest for small n , leading to larger induced η in the region closest to the wall, and hence larger induced radial velocity directed in towards the axis. For small n the vortex lines are emanating from the boundary layer at all radii and the

faster inwards radial velocity is larger for smaller n . Hence, the vortex lines at the edge of the boundary layer, where they are most inclined to the radial velocity, are swept radially inwards (see Fig. 9a), changing the sense of the curvature in Γ locally and inducing an extensive region of positive η inwards from the negative η region adjacent to the wall. For $n \geq 1$, this boundary layer process is not present. An analogous process occurs within the effusive corner region for all n considered, where the primary flow initially is more like solid-body rotation rather than a generalized potential vortex flow.

The results from computations over several values of n are summarized schematically in Fig. 13, showing a composite drawing of the vortex lines superimposed with the corresponding regions of azimuthal vorticity, for the two generic cases $n < 1$ (on the left and reflected) and $n > 1$ on the right half of the figure. The figure shows the relationship between the length scale r_c (the initial vortex core radius) and the radial extent of the effusive corner region r^* . The effusive corner region is schematically demarcated by the dashed line, and its radial extent, $r^*(t)$, is an increasing function of time. Initially, $r^*(t = 0) = r_c$. The

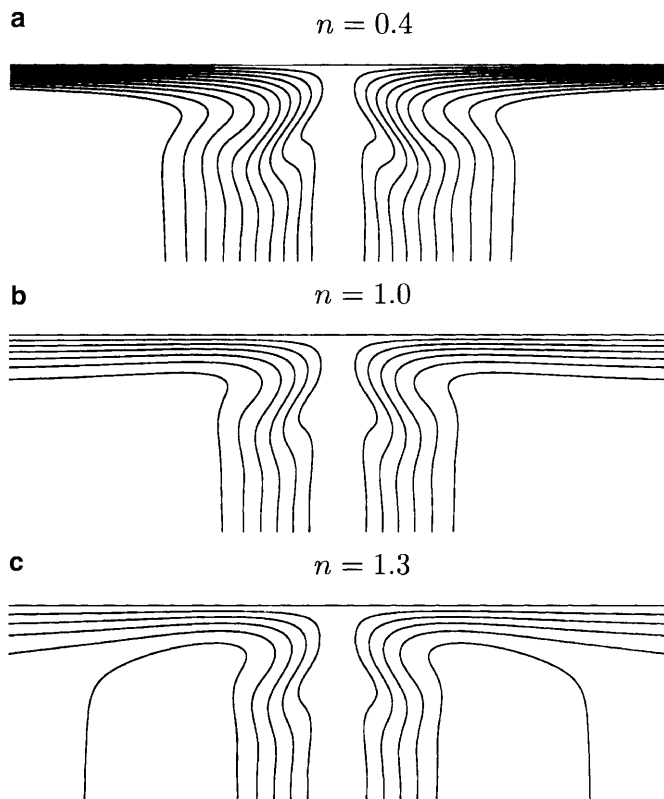


Fig. 9a-c. Contours of Γ (vortex lines) for $Re = 125$ at time $t = 20$ for various n indicated, in the effusive corner region ($R = 17.0$ and $Z = 25.5$). Contour levels are in uniform steps of 0.2

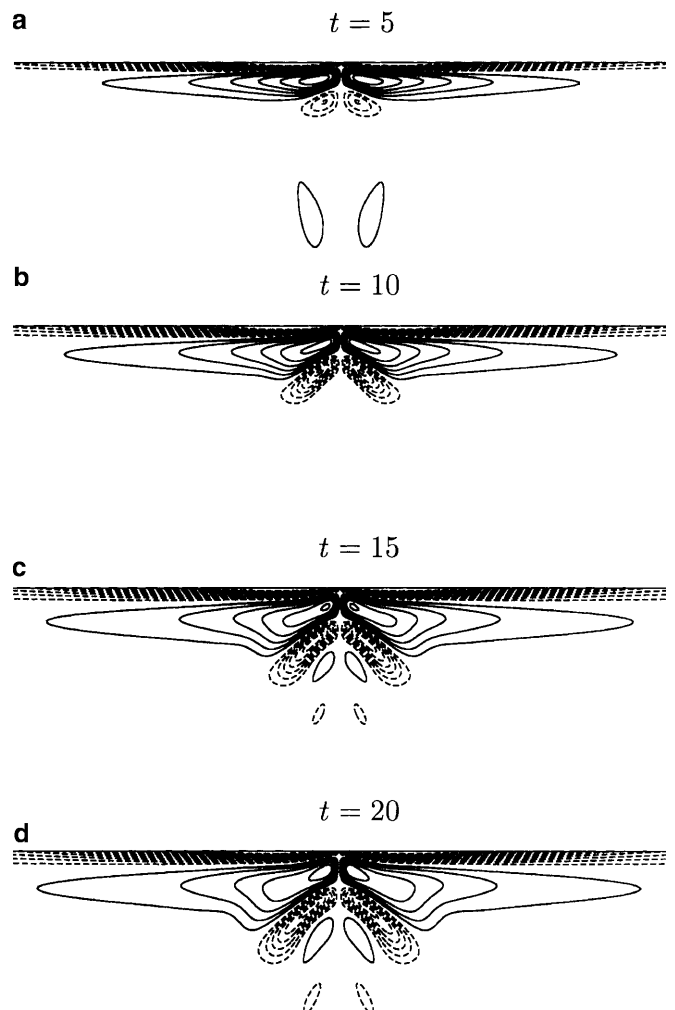


Fig. 10a-d. Contours of η for $Re = 125$, $n = 0.4$, and at various times as indicated, in the effusive corner region ($R = 17.0$ and $Z = 25.5$). Contours are set as in Fig. 8

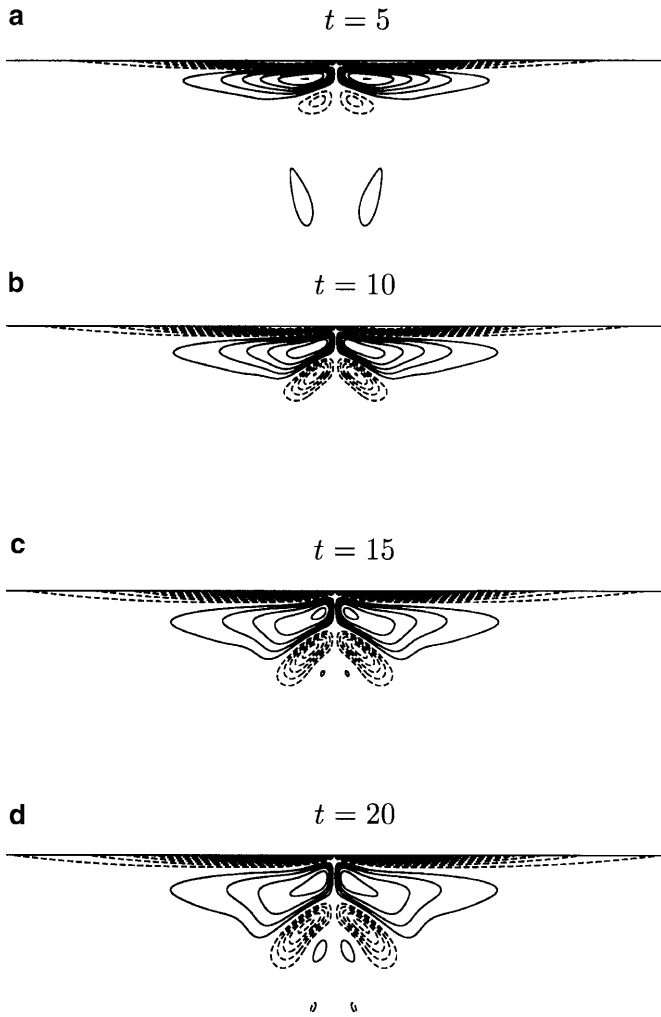


Fig. 11a-d. Contours of η for $Re = 125$, $n = 1.0$, and at various times as indicated, in the effusive corner region ($R = 17.0$ and $Z = 25.5$). Contours are set as in Fig. 8

figure also illustrates the correlation between vortex line curvature and the resultant azimuthal component of vorticity.

Even though the geometry of the experimental flow does not exactly match the axisymmetric geometry of the computations, primarily due to the presence of the flaps used to generate the initial vortex, there is a considerable correspondence between the primary features of the evolution in the effusive corner region of the two flows. From Fig. 7, we see that $\bar{z} = 1$ cm is the depth at which the induced η has its widest radial extent. Figure 5 gives the contours of the axial vorticity in a horizontal plane at depth 1 cm; from these we see that even though these contours are not circular, they are not as elliptical as one might expect given that the initial vortex profile corresponds to (1) with n varying from 0.4 to 1.3. The axisymmetric computations with $n = 0.4$ and 1.3 (Figs. 10 and 12) would have suggested that the contours of the axial vorticity in Fig. 5 should have been elliptical with major to minor axis ratio of about 2:1, whereas it is closer to about 5:4. The meridional plane in which the images for Fig. 7 were taken, with $\theta = 0^\circ$ and 180° , correspond to the $n = 0.4$ profile, which from the axisymmetric computa-

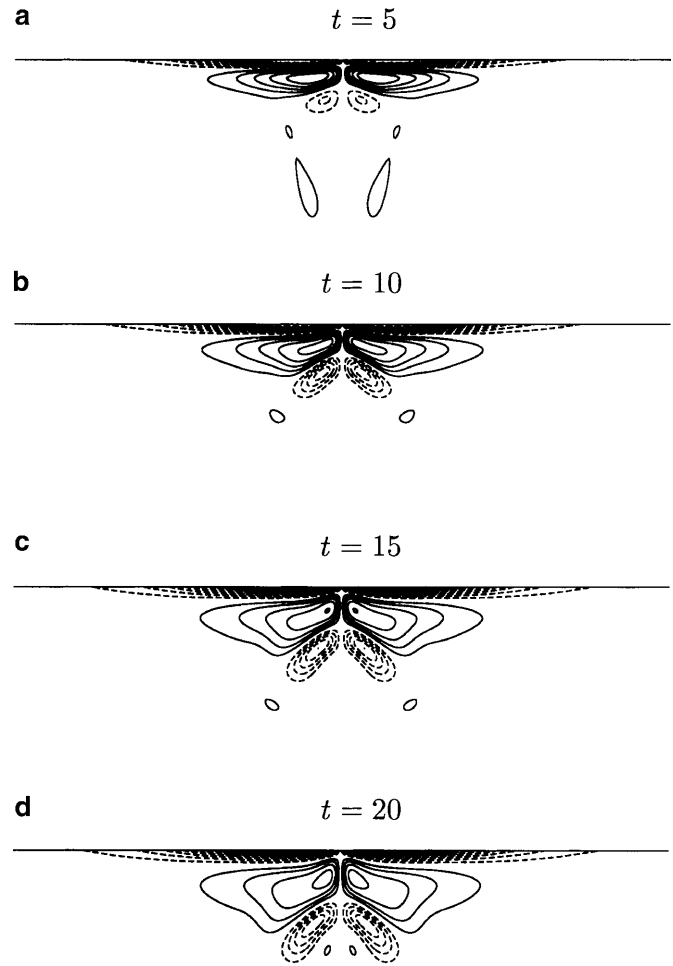


Fig. 12a-d. Contours of η for $Re = 125$, $n = 1.3$, and at various times as indicated, in the effusive corner region ($R = 17.0$ and $Z = 25.5$). Contours are set as in Fig. 8

tions with various n values, would be expected to have the largest radial extent for η , yet the contours of η in Fig. 7 correspond more closely to the $n = 1$ computations (Fig. 11). Overall, we have found computationally that the essential details of the interaction between the vortex and

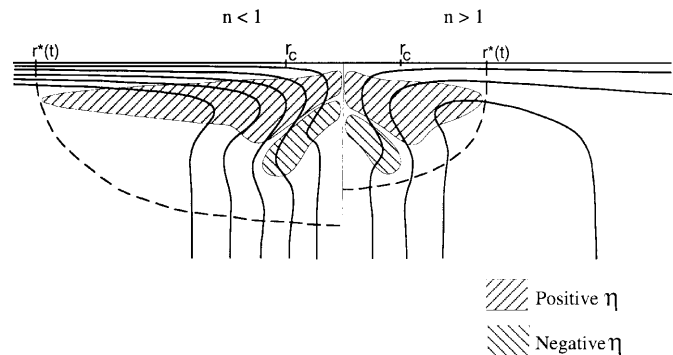


Fig. 13. Diagram showing the vortex lines (Γ) superimposed on the azimuthal vorticity (η) for latter stages of the interaction with the wall for $n < 1$ (left half and reflect) and $n > 1$ (right half); the data is from Figs. 9, 10 and 12. The effusive corner region is schematically shown by the dash line, the radial extent of which is $r^*(t)$; where r^* is initially equal to r_c

the wall are not greatly influenced by the value of n , and that the $n = 1$ axisymmetric computation at $Re = 125$ is quite representative of the experimental results.

5

Discussion and conclusions

The interaction between an initially columnar low Reynolds number vortex flow and a no-slip stationary wall normal to its axis in the region where the two meet is observed to be governed primarily by the local structure of the vortex. The geometry in which the flow resides provides only a higher order contribution to the early-time evolution. The general agreement between the experimental measurements and the axisymmetric computations in the effusive corner region from $t = 0$ up to at least $t = 20$ indicates that the essential dynamics in the effusive corner are axisymmetric and that the details of the far field do not control the early evolution. This agreement then allows the use of both the experimental and numerical results to elucidate the dynamics in the effusive corner.

The early inner core flow is essentially solid-body rotation, and the leading order behavior in the effusive corner region consists of the local interaction between a stationary no-slip wall and a swirling flow with an azimuthal velocity that is linear in r . This gives rise to the characteristic spatially oscillatory boundary layer structure associated with Bödewadt-type flows (Bödewadt 1940; also see Schlichting 1979; Lugt 1996). For these flows, the vortex lines leave the wall region in an oscillatory fashion, resulting from the advection of vortex lines by the secondary induced radial velocity near the wall. This in turn induces a region of positive radial velocity that sweeps the vortex lines radially outwards, inducing another region of negative radial velocity, and so on (also see Lopez and Weidman 1996; Lopez 1996). The amplitudes of these oscillations and the strength of the associated induced azimuthal vorticity are damped by viscous diffusion at low Re . Of secondary importance is the structure of the swirling flow outside the vortex core, characterized here by the parameter n . The subsequent evolution in this effusive corner region then differs from the Bödewadt-type flows, where the primary flow is essentially solid-body rotation for all radii, owing to the wall boundary layer at large r ($r > r^*(t)$) being of a potential vortex type.

We have found that the value of n influences the structure of the endwall boundary layer flow. The schematic of the vortex lines and the associated azimuthal component of vorticity for $n < 1$ and $n > 1$ was shown in Fig. 13, describing the vortex structure of the endwall boundary layer and the effusive corner region, as well as its extent. For a given Re , small n has a stronger induced radial inflow in the boundary layer than at large n . This radial inflow disrupts the Bödewadt-like boundary layer structure for $r < r_c$, but it is only a secondary effect. Further higher order effects are also induced by the geometry of the container; however, if the container is sufficiently large compared to the length scale of the initial vortex, then for early times the evolution of the interacting flow is essentially unaware of the confining geometry.

The prominent feature of the corner region observed in both the laboratory measurements and the numerical

simulations is the toroidal vortex structure. This structure is initiated at the wall (the Bödewadt structure for $r < r_c$) by vortex line bending and is consequently lifted differentially off the wall by the outer boundary layer flow as it turns into the axial direction in the effusive corner region. The lifting is greater for r closer to r_c than for r closer to 0 as the resulting axial velocity profile has a maximum away from $r = 0$. This results in a series of shear (azimuthal vorticity) layers (corresponding to the initial Bödewadt oscillatory layer), of alternating sign and diminishing strength, inclined to the wall. The shear layer closest to the wall extends out to large r and is bound to the wall. The second layer has a finite radial extent, of the order of the vortex core radius, and as it lifts off the wall it rolls up from its outer edge to form the observed toroidal vortex structure. At the Re in the present study, the other shear layers are quite weak and their evolution is dominated by viscous diffusion.

Finally, from the laboratory and numerical results, we find that the large toroidal structure does not develop from the columnar vortex itself, i.e. in the sense of vortex breakdown, but rather it develops from the endwall boundary layer structure as described above. This is clear from comparing the columnar structure of the vortex at late times when the endwall is not present (Fig. 4b) with the structure at early times when the endwall is present (Fig. 7). In the flow visualization experiments of Maxworthy (1972) and Phillips (1985), the appearance of the toroidal structure is more akin to the usual notion of vortex breakdown. Those experiments differ from the present study in that the meridional inflow is not only due to the wall interaction, but is augmented by an imposed meridional flow. Further study is needed to clarify this apparent difference in the dynamics.

References

- Belcher RJ; Burggraf OR; Stewartson K (1972) On generalized-vortex boundary layers. *J Fluid Mech* 52: 753–780
- Bödewadt UT (1940) Die Drehströmung über festem Grunde. *Z Angew Math Mech* 20: 241–245
- Burgers JM (1948) A mathematical model illustrating the theory of turbulence. *Adv Appl Mech* 1: 171–199
- Burggraf OR; Stewartson K; Belcher RJ (1971) Boundary layer induced by a potential vortex. *Phys Fluids* 14: 1821–1833
- Church CR; Snow JT; Baker GL; Agee EM (1979) Characteristics of tornado-like vortices as a function of swirl ratio: A laboratory investigation. *J Atmos Sci* 36: 1755–1766
- Fiedler BH (1994) The thermodynamic speed limit and its violation in axisymmetric numerical simulations of tornado-type vortices. *Atmosphere-Oceans* 32: 335–359
- Hama FR (1962) Streaklines in a perturbed shear flow. *Phys Fluids* 5: 644–650
- Hirsa A; Harper JE; Kim S (1995) Columnar vortex generation and interaction with a clean or contaminated free surface. *Phys Fluids* 7: 2532–2534
- Hirsa A; Korenowski GM; Logory LM; Judd CD (1997) Velocity field and surfactant concentration measurement techniques for free-surface flows. *Expt Fluids* 22: 239–248
- Howells P; Rotunno R; Smith RK (1988) A comparative study of atmospheric and laboratory-analogue numerical tornado-vortex models. *Q J R Meteorol Soc* 114: 801–822
- Howells P; Smith RK (1983) Numerical simulations of tornado-like vortices. Part 1: Vortex evolution. *Geophys. Astrophys Fluid Dyn* 27: 253–284

- Kim S** (1996) An experimental investigation of a columnar vortex terminating normal to a gas/liquid or a solid/liquid interface. Ph.D. Thesis, Rensselaer Polytechnic Institute
- Locke CA; Hirska A; Rubin MD** (1993) Short wave instability in a laminar vortex pair. In: Keith WL; Wei T (ed.) ASME Fluids Engineering Conference, Forum on Unsteady Flows. FED-Vol. 157, pp. 73–81, New York: American Society of Mechanical Engineers
- Logory LM; Hirska A; Anthony DG** (1996) Interaction of wake turbulence with a free surface. *Phys Fluids* 8: 805–815
- Lopez JM** (1996) Flow between a stationary and a rotating disk shrouded by a co-rotating cylinder. *Phys Fluids* 8: 2605–2613
- Lopez JM; Shen J** (1998) An efficient spectral-projection method for the Navier–Stokes equations in cylindrical geometries. *J Comput Phys* 139: 308–326
- Lopez JM; Weidman PD** (1996) Stability of endwall boundary layers during spin-down. *J Fluid Mech* 326: 373–398
- Lugt HJ** (1996) *Introduction to Vortex Theory*, Potomac MD: Vortex Flow Press
- Maxworthy T** (1972) On the structure of concentrated, columnar vortices. *Astronautica Acta* 17: 363–374
- Maxworthy T** (1973) A vorticity source for large-scale dust devils and other comments on naturally occurring columnar vortices. *J Atmos Sci* 30: 1717–1722
- Phillips WRC** (1985) On vortex boundary layers. *Proc R Soc Lond A* 400: 253–261
- Rott N** (1958) On the viscous core of a line vortex *Z angew Math Phys* 9b: 543–553
- Schlichting H** (1979) *Boundary-Layer Theory*, 7th ed, New York: McGraw-Hill
- Snow JT** (1982) A review of recent advances in tornado vortex dynamics. *Rev Geophys Space Phys* 20: 953–964
- Taylor GI** (1950) The boundary layer in the converging nozzle of a swirl atomizer. *Quart J Mech Appl Math* 3: 129–139
- Turner JS** (1966) The constraints imposed on tornado-like vortices by the top and bottom boundary conditions. *J Fluid Mech* 25: 377–400
- Ward WB** (1972) The exploration of certain features of tornado dynamics using a laboratory model. *J Atmos Sci* 29: 1194–1204
- Willert CE; Gharib M** (1991) Digital particle image velocimetry. *Expt Fluids* 10: 181–193
- Wilson T; Rotunno R** (1986) Numerical simulation of a laminar end-wall vortex and boundary layer. *Phys Fluids* 29: 3993–4005